

# Hard X-ray Photoelectron Spectroscopy at a Soft X-ray Source – Present and Future Perspectives of HAXPES at BESSY II

Running title: Hard X-ray Photoelectron Spectroscopy at a Soft X-ray Source – Present and Future Perspectives of HAXPES at BESSY II

Running Authors: Félix et al.

Roberto Félix <sup>1,a)</sup>, Mihaela Gorgoi <sup>1,2</sup>, Regan G. Wilks <sup>1,2</sup>, and Marcus Bär <sup>1-4</sup>

<sup>1</sup>Interface Design, Helmholtz-Zentrum Berlin für Materialien und Energie GmbH, 12489 Berlin, Germany

<sup>2</sup>Energy Materials In-Situ Laboratory Berlin (EMIL), Helmholtz-Zentrum Berlin für Materialien und Energie GmbH, 12489 Berlin, Germany

<sup>3</sup>Helmholtz-Institute Erlangen-Nürnberg for Renewable Energy (HI ERN), 12489 Berlin, Germany

<sup>4</sup>Department of Chemistry and Pharmacy, Friedrich-Alexander-Universität Erlangen-Nürnberg, 91054 Erlangen, Germany

a) Electronic mail: [roberto.felix\\_duarte@helmholtz-berlin.de](mailto:roberto.felix_duarte@helmholtz-berlin.de)

Hard x-ray photoelectron spectroscopy (HAXPES) is a powerful technique to characterize the chemical and electronic structure of materials. In energy conversion devices, often composed of a stack of thin layers and thus containing multiple buried interfaces, the increased probing depth of HAXPES, compared to conventional x-ray photoelectron spectroscopy, makes it a technique of choice to ultimately reveal a more comprehensive device-relevant picture. In this contribution, we provide a brief review on recent HAXPES experiments conducted at the High Kinetic Energy Photoelectron Spectrometer (HiKE) endstation located at the BESSY II KMC-1 beamline at Helmholtz-Zentrum Berlin für Materialien und Energie GmbH (HZB), focusing on three different prominent sample material systems widely used in energy conversion devices: i) Cu-chalcogenides, ii) metal oxides, and iii) halide perovskites. The findings revealed by these studies highlight the advantage of knowledge-based heterointerface design in

energy conversion devices, building interface models based on direct measurements targeting the entire structure as only possible by HAXPES. We conclude by giving an update on the new and enhanced HAXPES experimental capabilities starting to be offered by the Energy Materials In-situ Laboratory Berlin (EMIL) facility.

## I. INTRODUCTION

The Helmholtz-Zentrum Berlin für Materialien und Energie GmbH (HZB) operates the BESSY II synchrotron light source, a 1.7 GeV ring with a critical energy of  $\approx 2.5$  keV. While optimized for lower energies, there is considerable utility in exploiting the higher energy regions on a limited number of beamlines to enable measurements in the tender-to-hard x-ray regime on-site. For the past years, this niche of tender-to-hard x-ray photoelectron spectroscopy has been filled at BESSY II by the High Kinetic Energy Photoelectron Spectrometer (HiKE) endstation at the KMC-1 bending magnet beamline,<sup>1,2</sup> and these capabilities are being further expanded with the construction and commissioning of the two-color EMIL beamline of the Energy Materials In-situ Laboratory Berlin (EMIL), which allows continuous variation of the photon energy over the range of approximately 80 eV – 10 keV using two canted undulators.<sup>3,4</sup> In this work, we will outline contributions to energy materials research using tender and hard x-ray photoelectron spectroscopy at BESSY II in recent years as well as provide a look to the future.

The multitude of layers, interfaces, surfaces, elements, impurities, etc. contributing to the structure, function, and performance of energy conversion devices means that characterization and fundamental understanding of the chemical and

electronic structures of each component, as well as their interactions, are crucial to support technical progress.<sup>5-18</sup> Hard x-ray photoelectron spectroscopy (HAXPES) provides a means of extending the information gathered from conventional photoelectron spectroscopy below the immediate surface of the material and toward the bulk – including buried interfaces.<sup>18</sup> Variation of excitation energy, and therefore the scattering profile of the photoelectrons, is a straightforward approach to nondestructively analyze potential elemental depth profiles of material multilayer systems. The overall increase of probing depth when using hard x-rays aids in the execution of in-situ experiments mimicking conditions of treatment steps employed in the preparation of “real-world” devices (e.g., in-situ annealing treatment) while monitoring the properties of the near-surface material bulk or buried interfaces, which can yield valuable information that can help build knowledge-based strategies to improve the component and/or performance of a device.

In this contribution, we provide a brief review on recent publications based on HAXPES experiments conducted at the HiKE endstation located at the BESSY II KMC-1 beamline at HZB.<sup>1,2</sup> The endstation is equipped with a Scienta R4000 electron analyzer, with an optimized photoelectron kinetic energy range of 0.15 – 10 keV, allowing it to use the 2 – 10 keV excitation energy range provided by the KMC-1 bending magnet beamline. The KMC-1 double crystal monochromator (DCM) can make use of three different monochromator crystal pairs: Si(111), Si(311) and Si(422), depending on the desired excitation energy and other experimental requirements. As a standard experimental procedure, multiple diffraction orders (e.g., 2 keV in 1st order and 6 keV in 3rd order) of the Si(111) crystal pair of the DCM are used to enable fast switching

between excitation energies while maintaining similar energy resolution. (Although Si(333) provides 6 keV photons with a narrower linewidth [i.e.,  $(0.05 \pm 0.02)$  eV] than Si(111) 2 keV photons [i.e.,  $(0.21 \pm 0.01)$  eV], the total energy resolution is, for these two settings, mostly determined by the resolution of the electron analyzer. For the measurements discussed below, an electron analyzer pass energy of 200 eV was used, resulting in a total energy resolution of  $(0.30 \pm 0.05)$  eV).<sup>1,2</sup> To prevent beam damage effects on sensitive samples, measurements can be conducted with beam attenuating filters. (For more details on the KMC-1 beamline technical specifications, please refer to ref. <sup>2</sup>). The publications discussed in this work are examples from our group showcasing the power of HAXPES, even if performed on a bending magnet beamline on a storage ring dedicated to produce highly brilliant soft x-rays. Data on three different prominent sample material systems widely used in energy conversion devices is presented: i) Cu-chalcogenides, ii) metal oxides, and iii) halide perovskites. We conclude by giving an update/perspective on the EMIL facility, discussing the new and enhanced HAXPES experimental capabilities starting to be offered there to the international user community.

## II. COPPER CHALCOGENIDES

Cu-chalcogenides, with  $\text{Cu}(\text{In}_{1-x}\text{Ga}_x)(\text{S}_y\text{Se}_{1-y})_2$  (CIGSSe) chalcopyrites and  $\text{Cu}_2\text{Zn}(\text{Sn,Ge})(\text{S,Se})_4$  (CZTGSSe) kesterites as the most prominent representatives from the field of photovoltaics (PV), are used as light absorber materials in thin-film solar cells. In this section, a brief introduction to these absorber material classes is given, pointing out the current advantages and disadvantages of them. As absorbers based on these material systems often show differences in elemental composition at the surface

compared to their bulk (e.g., depth-dependent element profiles, presence of secondary phases at the surface, etc.), HAXPES is an effective technique to ascertain the influence of such features on the performance of resulting solar devices. Examples of HAXPES research conducted on chalcopyrite and kesterite samples to better understand relevant open questions about these systems are provided.

## **A. Chalcopyrites**

Solar cells based on chalcopyrite CIGSSe absorbers have demonstrated lab-scale performance conversion efficiencies ( $\eta$ ) above 23% (record  $\eta$ : 23.4%),<sup>19</sup> with record devices containing absorbers with an average composition of  $x \approx 0.3$  and  $y = 0$  [ $\rightarrow$  Cu(In<sub>1-x</sub>Ga<sub>x</sub>)Se<sub>2</sub>: CIGSe], resulting in bulk-sensitive optical band gap ( $E_g$ ) values of  $\approx 1.2$  eV. The possibility of tuning the  $E_g$  of the absorber by selecting its elemental composition to better match the optimum absorber  $E_g$  for terrestrial solar energy conversion has been an attractive feature of this material system. For years, advances in efficiency for this type of device have taken place as a result of empirical optimization of the synthesis process of the device. At the current stage of chalcopyrite PV development, nearing the efficiency limit of  $\approx 30\%$  for a single p-n junction solar cell according to the Shockley-Queisser model,<sup>20</sup> it is apparent that further advancement in device performance will require knowledge-based optimization strategies.

For example, the beneficial effects of diffusion of Na from the soda lime glass back contact into the absorber layer, induced by high temperature steps during sample preparation, has long been established.<sup>21,22</sup> In low temperature sample preparation processes or when Na-free substrates are used, the deliberate supplying of Na as part of

the sample production recipe has become a standard procedure in order to achieve suitable device performances.<sup>23</sup> After a period of time when the efficiency of such devices appeared to have plateaued, a boost in the record conversion efficiencies was achieved by deliberately submitting CIGSe absorbers to post deposition treatments (PDT) with alkali fluorides.<sup>24,25</sup> The PDT process beneficially modifies the optoelectronic properties of the CIGSe absorber and provides an improved surface for buffer layer deposition,<sup>26-28</sup> allowing the CdS buffer thickness to be reduced without significant losses in device performance, while increasing the device's short-circuit current density ( $J_{SC}$ ) due to a reduction in parasitic absorption in the ultraviolet wavelength region.

The impact of NaF-, NaF/KF-, and NaF/RbF PDT on the chemical and electronic structure of CIGSe has been investigated via HAXPES by Handick et al.<sup>5,6,29</sup> and Bombsch et al.<sup>7</sup> In general, the chemical structure of the treated samples is transformed with the formation of a nanopatterned Alkali-In-Se-type compound (e.g., K-In-Se- and Rb-In-Se-type compounds for NaF/KF- and NaF/RbF PDT, respectively) and by heavy Cu-depletion at the sample's surface. As a result of these sample surface modifications, the  $E_g$  at the surface of PDT samples widens compared to samples without treatment. Moreover, the thickness and degree of nanopatterning produced by the PDT can be tuned by the parameters of the treatment (e.g., evaporation rate of the alkali fluoride).

The chemical and electronic properties of the heterointerface formation between an RbF-PDT CIGSe absorber and a CdS buffer layer, as investigated by HAXPES, has been reported by Nicoara et al.<sup>8</sup> Figure 1 shows HAXPES spectra of the (a) Cd  $3d_{5/2}$  and (b) Rb 3p, Se 3s, S 2s energy regions for RbF-PDT CIGSe treated with varying CdS chemical bath deposition (CBD) times. Although Cd is found in the sample with the

shortest CBD treatment (i.e., 1 s), the broader Cd 3d<sub>5/2</sub> peaks observed for samples with CBD treatments shorter than 3 minutes denote the presence of several Cd chemical species. This result, in addition to the detection of the presence of Rb and Se-O and/or S-O in samples with CBD treatments shorter than 3 minutes, altogether reveals the highly heterogenous chemical environment found in near heterointerface region. These findings reveal the limits to CdS layer thickness reduction elicited by PDT, with shorter deposition treatments resulting in buffer layers with highly nonuniform structures, the properties of which can degrade the efficiency of resulting devices.

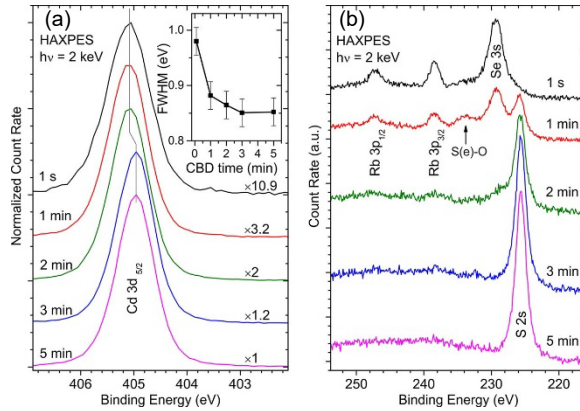


FIG. 1. HAXPES spectra of the (a) Cd 3d<sub>5/2</sub> and (b) Rb 3p, Se 3s, S 2s energy regions for RbF-PDT CIGSe treated with varying CdS chemical bath deposition (CBD) times. An excitation energy of 2 keV was employed. *Reprinted with permission from ref. <sup>8</sup>. Copyright 2017 American Chemical Society.*

## B. Kesterites

The CZTGSSe kesterite material system is a less mature technology than CIGSe; however, it is of great interest as it uses non-toxic and earth-abundant elements, as well

as, allowing for  $E_g$  tuning capabilities between 1.0 (for  $\text{Cu}_2\text{ZnSnSe}_4$ , CZTSe) and 2.3 eV (for  $\text{Cu}_2\text{ZnGeS}_4$ , CZGS) by changing its elemental composition (similar to chalcopyrites, as discussed above).<sup>30,31</sup> Another attractive feature is that the highest performance kesterite solar devices have been based on absorbers prepared through solution-based deposition, which can streamline production to a larger scale with greater ease. To date, solar cell devices made with narrow band gap (1.13 eV)  $\text{Cu}_2\text{ZnSn}(\text{S},\text{Se})_4$  (CZTSSe) absorbers have achieved a record  $\eta$  of 12.6 %, <sup>19</sup> exhibiting significantly lower performances than their CIGSe-based counterparts (discussed above). This lag in performance is related to a significant deficit in open circuit voltage ( $V_{OC}$ ) compared to the maximum  $V_{OC}$  value predicted by the Shockley-Queisser radiative limit ( $V_{OC,SQ}$ ),<sup>20</sup> with  $V_{OC}$  of kesterite devices being unable to surpass 60% of  $V_{OC,SQ}$ , while corresponding  $J_{SC}$  and fill factors (FF) values are greater than 80% of their maximum limits. Improvement in the limiting parameter (i.e.,  $V_{OC}$ ) is necessary in order to bridge performances of kesterite-based devices and prominent PV technologies. In the work by Vermang et al.<sup>9</sup> and Choubrac et al.<sup>10</sup>, substitution of Sn by Ge is explored as a strategy to overcome the  $V_{OC}$  deficit of kesterite solar devices. In the preparation of  $\text{CuZnGeSe}_4$  (CZGSe) films, the formation of a ZnSe secondary phase was detected at the surface of the investigated samples, which acted as a barrier for the transport of charge carriers across the absorber/buffer heterointerface. (This scenario is consistent with the observed  $V_{OC}$  deficit, as non-optimized heterointerfaces in solar devices, especially the absorber/buffer interface, can open routes to charge carrier recombination losses.) Different surface treatments were developed to etch away (with hot HCl) the performance-inhibiting ZnSe phase and to passivate the etched surface with aqueous

(NH<sub>4</sub>)<sub>2</sub>S, a solution that mimics the chemical situation in the early stages of the buffer layer chemical bath deposition environment on the surface and near-surface chemical structure of the sample. Figure 2 shows HAXPES spectra of the (a) Se 3d and (b) Ge 3d energy regions, including curve fit analysis results. These results demonstrate that the ZnSe phase present at the as-grown CZGSe sample surface is effectively removed by the hot HCl etching step; however, this treatment results in the appearance of new Se- and Ge-related signal, likely indicating the formation of a Ge-Se species, which requires the aqueous (NH<sub>4</sub>)<sub>2</sub>S based surface passivation treatment to be removed.

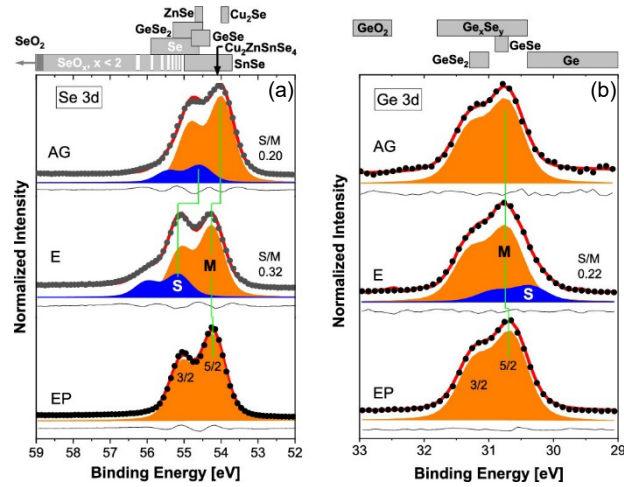


FIG. 2. HAXPES spectra of the (a) Se 3d and (b) Ge 3d energy regions, including curve fit analysis results and reference binding energy positions, of CZGSe absorbers with the following treatments: as-grown (AG); etched in hot HCl (E); and etched in HCl followed by passivation in ammonium sulfide solution (EP). An excitation energy of 2.1 keV was employed. *Reprinted with permission from ref. <sup>10</sup>. Copyright 2020 American Chemical Society.*

### III. METAL OXIDES

Metal oxides (MOs) possess material properties that make them extremely useful in various electronic devices, such as tunable electronic properties, high transparency in the visible range, and stable chemical structure in ambient environment.<sup>32,33</sup> For example, they are incorporated as interfacial materials in energy conversion devices (e.g., water splitting and PV devices)<sup>34</sup> and show promising potential in ferroelectric applications.<sup>35</sup> Examples of studies conducted on samples related to these applications are provided in the following.

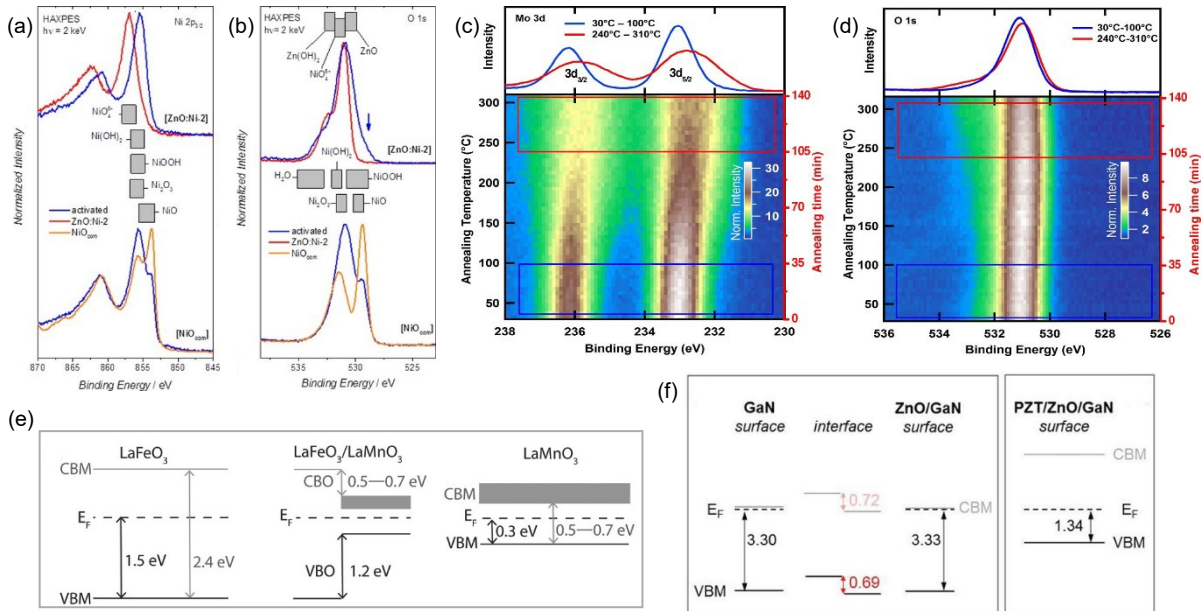


FIG. 3. HAXPES spectra of the (a) Ni 2p<sub>3/2</sub> and (b) O 1s energy regions for as-prepared and activated commercial NiO (labeled “[Ni<sub>com</sub>]”) and ZnO:Ni nanoparticle (labeled “[ZnO:Ni-2]”) samples, including reference binding energy positions. An excitation energy of 2 keV was employed. *Reprinted with permission from ref. <sup>11</sup>. Copyright 2017*

*Wiley-VCH Verlag GmbH & Co. KGaA, Weinheim.* Evolution of HAXPES spectra of the (c) Mo 3d and (d) O 1s energy regions of MoO<sub>3</sub>, shown as 2D intensity maps as a function of annealing temperature (and therefore time). The upper panels show the sum of spectra measured in the stated temperature ranges. An excitation energy of 2 keV was employed. *Reprinted with permission from ref. <sup>14</sup>. Copyright 2019 American Chemical Society.* Experimentally-determined energy level alignment of the heterointerfaces found in the (e) LaFeO<sub>3</sub>/LaMnO<sub>3</sub> and (f) Pb(Zr<sub>0.2</sub>,Ti<sub>0.8</sub>)O<sub>3</sub>(PZT)/ZnO/GaN stacks. These structures were determined from measurements employing excitation energies of 6 and 2 keV, respectively. *Reprinted with permission from ref. <sup>12</sup>. Copyright 2017 Wiley-VCH Verlag GmbH & Co. KGaA, Weinheim.* *Reprinted with permission from ref. <sup>13</sup>. Copyright 2020 Wiley-VCH Verlag GmbH & Co. KGaA, Weinheim.*

## **A. Water oxidation catalysts**

Hydrogen generated from water is proposed as a potential vector for the storage of PV-generated energy. To date, the most effective water oxidation catalysts (WOC) are based on precious metals, making the development of more cost-effective catalysts based on earth-abundant metals a topic of great research interest.  $\gamma$ -NiOOH is the most active phase for water oxidation of the highly effective WOC based on nickel(III) oxo-hydroxo species.<sup>36</sup> A drawback of  $\gamma$ -NiOOH is that it ages into the less active  $\beta$ -Ni(OH)<sub>2</sub> phase. Pfrommer et al. report on the production of WOC electrodes based on heterobimetallic Ni-substituted ZnO (ZnO:Ni) nanoparticles that support the formation of NiOOH, after a period of activation by continued cycling.<sup>11</sup> The chemical structure of ex situ prepared and activated heterobimetallic ZnO:Ni and homometallic NiO samples were examined

via HAXPES. The greater probing depth of HAXPES measurements, compared to lab-based x-ray photoemission spectroscopy, makes it an ideal tool to examine ex situ samples covered by adsorbates due to exposure to electrochemical solutions. Figure 3 shows the HAXPES spectra of the samples in the (a) Ni 2p<sub>3/2</sub> and (b) O 1s energy regions. Based on the features of the Ni 2p<sub>3/2</sub> and O 1s spectra of the as-prepared commercial NiO sample (labeled “[Ni<sub>com</sub>]” in the figure) show, unsurprisingly, the predominant NiO chemical environment of the sample. Upon activation, there is a small remainder of NiO, having transformed to Ni<sub>2</sub>O<sub>3</sub> and/or Ni(OH)<sub>2</sub> with possibly a small amount of NiOOH. For the as-prepared ZnO:Ni nanoparticle sample (labeled “[ZnO:Ni-2]” in the figure), the Ni 2p<sub>3/2</sub> and O 1s spectra reveal the presence of ZnO, Zn(OH)<sub>2</sub> and NiO<sub>4</sub><sup>6-</sup>-type environments. After activation (with a significant amount of Zn dissolving during the process), clear evidence of the formation of NiOOH is detected in the activated ZnO:Ni sample. These chemical characterization results are in complete agreement with the electrocatalytic performance observed for the samples (i.e., a gradual activity deterioration for the NiO system vs a steadily increasing catalytic output over time for the ZnO:Ni system).

## ***B. Hole transport materials***

Despite the excellent behavior of MoO<sub>3</sub> as a hole transport material (HTM) in organic solar cells (OSC) and organic light-emitting diodes (OLED), efforts to implement MoO<sub>3</sub> as an HTM in hybrid organic-inorganic perovskite (HOIP) solar devices have been less successful. The underlying reason has been conjectured to be the deep valence band maximum (VBM) position of MoO<sub>3</sub>, which may act as a barrier for hole transport,<sup>37</sup> with

the introduction of in-gap states in MoO<sub>3</sub> being proposed as a potential solution.<sup>38</sup> Tunability of the chemical and electronic properties of MoO<sub>3</sub> by sample annealing treatment has been investigated in situ via HAXPES by Liao et al.<sup>14</sup> Figure 3 displays the changes in the (c) Mo 3d and (d) O 1s energy region as a function of annealing temperature (and therefore time). Annealing the MoO<sub>3</sub> sample from room temperature to around 100 °C seems to induce no change in the Mo 3d doublet peaks. Increasing the annealing between a temperature range of 100 – 240 °C results in the line shape of the peaks broadening (becoming asymmetric) and shifting towards lower binding energy values, indicating the formation of Mo<sup>5+</sup> (at around 120°C) and Mo<sup>4+</sup> (at around 200 °C) chemical species. These results are in agreement with changes in the O 1s energy region as a function of annealing temperature. In addition to the main O 1s contribution found at 530.5 eV and ascribed to a MoO<sub>3</sub> oxygen environment, two new O 1s contributions emerge at approximately the same annealing temperatures at which the Mo<sup>5+</sup> and Mo<sup>4+</sup> species are detected in the Mo 3d lines. These two oxygen contributions are detected at 531.7 eV and 533.1 eV and are ascribed to environments of molybdenum suboxides or oxygen vacancies. Moreover, density of states (DOS) emerge at energies of 0.8 and 1.8 eV below the Fermi level (E<sub>F</sub>) level (not shown, however, we refer the reader to Fig. 3 of ref. <sup>14</sup>), attributed to partially occupied d bands of Mo<sup>5+</sup> and Mo<sup>4+</sup>, respectively.<sup>37</sup> As the VBM of the MoO<sub>3</sub> sample is found at (3.0 ± 0.1) eV below E<sub>F</sub>, these newly-formed DOS intensities are in-gap states resulting from the annealing treatment. These results demonstrate the effective way to deliberately tune the chemical and electronic properties of physical vapor deposited MoO<sub>3</sub> based on sample annealing. Despite the possibility of introducing in-gap states the electronic structure of MoO<sub>3</sub>, its implementation as a hole

transport material in HOIP solar devices continues to be unfeasible for reasons discussed in the next section (see Sect. IV.A). However, this is a clear example of a HAXPES-enabled in-situ experiment exploring treatment parameters for the conditioning of a device component that can affect the performance of the entire device.

### **C. Charge transfer controlling interfaces**

To better understand the electronic properties of heterojunctions based on semiconductor oxides, in which charge transfer across the interface can take place and/or be manipulated, sample series based on the  $\text{LaFeO}_3$ (LFO)/ $\text{LaMnO}_3$ (LMO) and  $\text{Pb}(\text{Zr}_{0.2},\text{Ti}_{0.8})\text{O}_3$ (PZT)/ $\text{ZnO}/\text{GaN}$  heterointerfaces were investigated via HAXPES in order to determine their heterointerface energy level alignments.<sup>12,13</sup> The ferrite/manganite (LFO/LMO) heterointerface is considered a strong candidate structure for spintronic applications. Likewise, the PZT/ $\text{ZnO}/\text{GaN}$  stack, which contains ferroelectric/semiconductor heterostructures, has garnered attention for opening a new route in the development of next-generation tunable resistive memory devices. Figure 3(e) and (f) displays the energy level alignment of both systems, respectively, as revealed by the HAXPES results and optical band gap measurements.

The LFO/LMO heterointerface exhibits a type I (straddling) energy level alignment, in which the VBM and conduction band minimum of the LFO component are further away from  $E_F$  than the ones for the LMO component. The reported valence band offset (VBO) and conduction band offset (CBO) are  $(1.20 \pm 0.07)$  eV and  $(0.5-0.7 \pm 0.3)$  eV, respectively. Moreover, no significant change is observed in the binding energy position or in the shape of the Fe 2p and Mn 2p core level spectra of the investigated

LFO/LMO thickness series with increasing LFO thickness, indicating no significant interface induced band bending and the retention of the 3+ oxidation state for both Fe and Mn. These findings demonstrate the absence of charge transfer across the investigated heterointerface, which stands in contrast to the properties of other LMO-based heterojunctions. In Figure 3(e), the experimentally-determined energy level alignment of the heterointerfaces found in the PZT/ZnO/GaN stack is displayed. Type II (staggered) band structures are detected for the PZT/ZnO and ZnO/GaN interfaces. The ZnO/GaN component shows VBO and CBO values of  $(0.69 \pm 0.14)$  eV and  $(0.72 \pm 0.14)$  eV, respectively. A precise energy level alignment at the PZT/ZnO interface is not possible (for reasons discussed in ref. <sup>13</sup>); however, the VBO and CBO can be estimated to be between 1.7 – 2.0 eV and 2.0 eV, respectively; values significantly larger than suggested from electron affinity values from literature.<sup>39,40</sup> The large offsets exhibited by this and the LFO/LMO heterointerface (discussed above) are in line with systems capable of strong carrier separation/confinement. The findings revealed by these studies highlight the advantage of building interface models based on direct measurements targeting the entire structure, as facilitated by HAXPES, rather than on estimates based on the bulk properties of individual material components.

## IV. HALIDE PEROVSKITES

Photovoltaic devices based on hybrid organic-inorganic perovskites (HOIP) using  $\text{APbX}_3$  [ $\text{A} = \text{CH}_3\text{NH}_3^+$ ,  $\text{HC}(\text{NH}_2)_2^+$ ,  $\text{Cs}^+$  and  $\text{X} = \text{I}^-$ ,  $\text{Cl}^-$ ,  $\text{Br}^-$ ] as the absorber layer have demonstrated rapid and sustained improvements in device efficiency. Lab-scale solar cells using HOIP absorbers have reached  $\eta$  exceeding 25% (record  $\eta$ : 25.5%),<sup>19</sup> on par

(or above) established solar cell technologies based on chalcopyrites (discussed in Sect. II.A), CdTe, and multicrystalline Si wafer absorbers. Similar to kesterite-based absorbers (discussed in Sect. II.B), the synthesis of HOIP absorber can be based entirely on relatively simple (compared to the preparation of other absorber materials employed in solar device configurations) wet-chemistry processes. Despite these definite advantages, HOIP-based solar devices face formidable challenges that hinder their upscaling and commercialization.<sup>41</sup> Many formulations exhibit rapid performance deterioration associated with internal (e.g., composition-related defects, ion migration, etc.)<sup>15</sup> and external instabilities (e.g., degradation due to exposure to moisture, heat, light, oxygen, etc.).<sup>42-45</sup> Moreover, high-performance devices are based on Pb-containing HOIP absorber, a fact that raises environmental concerns for implementation goals at a larger scale. Efforts to substitute Pb with a less regulated and more environmentally friendly element are underway. However, the highest performances for Pb-free HOIP solar devices, which are obtained with Sn-based HOIP absorbers (record  $\eta$ : 13.24%),<sup>46</sup> are significantly lower. This apparent setback is linked to the greater ease of Sn to oxidize (i.e.,  $\text{Sn}^{2+}$  to  $\text{Sn}^{4+}$ ) compared to Pb (i.e.,  $\text{Pb}^{2+}$  to  $\text{Pb}^{4+}$ ), bringing a new instability factor to consider.

In the following, the results of the chemical structure characterization of a HOIP/MoO<sub>3</sub> (absorber/HTM) heterointerface are considered, serving as an example of degradation cascades that can take place in non-optimal interface structures and highlighting the importance of knowledge-based heterointerface design in HOIP solar devices. Moreover, as a recent strategy to prevent or minimize the impact that the above-mentioned defects have on the performance of HOIP-based solar devices is to include

metal halide salt additives during sample preparation, the results of HAXPES studies on the effect of these additives on the chemical and electronic structures of Pb- and Sn-based absorbers are also presented.

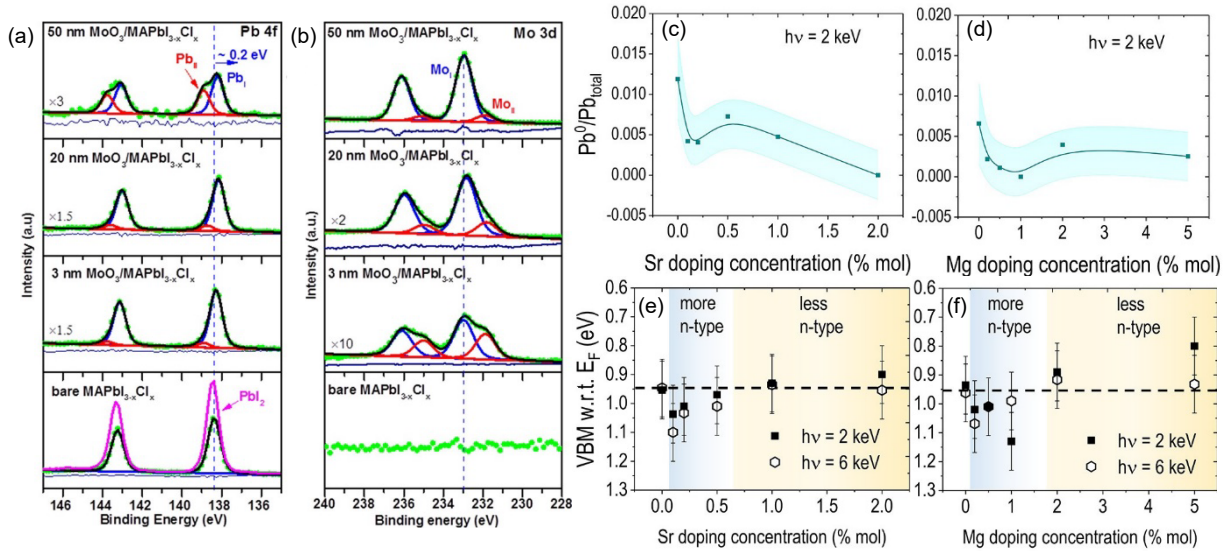


FIG. 4. HAXPES spectra of the (a) Pb 4f and (b) Mo 3d energy regions of  $\text{MAPbI}_{3-x}\text{Cl}_x$  before (bare) and after deposition of  $\text{MoO}_3$  layers of nominal thicknesses of 3, 20, and 50 nm produced by physical vapor deposition, including curve fit analysis results. An excitation energy of 2 keV was employed. *Adapted with permission from ref. 17.*

*Copyright 2021 American Chemical Society.* HAXPES-derived fraction of metallic Pb compared to total Pb content ( $\text{Pb}^0/\text{Pb}_{\text{total}}$ ) of (c) Sr-doped and (d) Mg-doped  $\text{MAPbI}_3$  samples, as a function of nominal dopant concentration. Evolution of VBM position with respect to  $E_F$  of (e) Sr-doped and (f) Mg-doped  $\text{MAPbI}_3$  samples, as a function of nominal dopant concentration. The values were determined from measurements employing excitation energies of 2 and 6 keV. *Adapted with permission from ref. 15.*

*Copyright 2020 American Chemical Society.*

## **A. Chemical structure of MoO<sub>3</sub>/HOIP heterointerface**

As already discussed in Sect. III.B, MoO<sub>3</sub> is one of the most widely used HTM in organic solar cells; however, its implementation as a HTM in HOIP solar devices has not been successful. The reason behind this shortcoming has been associated with a non-optimized energy level alignment at the HTM/HOIP heterointerface, especially the VBO.<sup>37</sup> However, this hypothesis fails to consider the chemical reactivity resulting from contact between the HOIP absorber and MoO<sub>3</sub>. The chemical structure of the MoO<sub>3</sub>/HOIP heterointerface was investigated via HAXPES by Liao et al.<sup>17</sup>, which demonstrates the highly reactive character of the heterointerface. Figure 4 presents HAXPES spectra in the (a) Pb 4f and (b) Mo 3d energy regions for MAPbI<sub>3-x</sub>Cl<sub>x</sub> (MA = CH<sub>3</sub>NH<sub>3</sub><sup>+</sup>) samples with different MoO<sub>3</sub> thicknesses produced by physical vapor deposition. Clear signs of the formation of new Pb and Mo chemical species can be observed by the appearance of new peaks in the spectra (it is noted that similar results are detected for the I 3d, N 1s, O 1s, and C 1s lines), highlighting the strong chemical interaction taking place at both the absorber and the HTM sides (for the identification of the newly formed chemical species and the suggested chemical reaction pathways, please refer to the ref. <sup>17</sup>). These findings reveal that the severe decomposition of the MAPbI<sub>3-x</sub>Cl<sub>x</sub> absorber as a result of the direct contact by the MoO<sub>3</sub> layer is responsible for the performance of HOIP solar devices including MoO<sub>3</sub> as the HTM.

## **B. Effect of metal halide additives on Pb-based HOIP**

To reduce the concentration of defects present in HOIP absorbers (e.g., halide vacancies and interstitials),<sup>47</sup> which recent studies have shown to be the origin of many degradation pathways,<sup>48</sup> metal halides (e.g., SrI<sub>2</sub> and MgI<sub>2</sub>) are used as additives in the preparation of HOIP absorbers. The additives supposedly passivate HOIP defects by producing a halide-rich precursor solution and by introducing Sr<sup>2+</sup> and Mg<sup>2+</sup> dopant interstitials in the absorber lattice that increase the energy barrier for halide migration.<sup>49,50</sup> The chemical composition and electronic properties of MAPbI<sub>3</sub> sample series treated with SrI<sub>2</sub> and MgI<sub>2</sub> additives were studied via HAXPES by Phung et al.<sup>15</sup>, in which the prevalence of metallic Pb<sup>0</sup> was used to monitor changes in defect concentration in the films. The investigated samples showed optical E<sub>g</sub> values of ≈1.6 eV. Figure 4(c)-(f) presents HAXPES-derived quantifications of the Pb<sup>0</sup>-to-total-Pb content (Pb<sup>0</sup>/Pb<sub>total</sub>) and the determined VBM values of the samples as a function of additive concentration. Reductions in defect concentration, as assessed by the Pb<sup>0</sup>/Pb<sub>total</sub> values, are seen for all treated samples; however, correlations between changes in Pb<sup>0</sup>/Pb<sub>total</sub> values and VBM shifts of the samples are only detected up to a dopant cation concentration. This suggests that there is a threshold for dopant incorporation into the absorber lattice above which it starts to segregate at the surface of the sample. Additive treatments with concentrations below or at the threshold result in materials with more n-type doping character, while treatments with concentrations above the threshold result in materials with less n-type doping character. Moreover, the concentration threshold depends on the size of the dopant cation, with the smaller cation radius (i.e., Mg<sup>2+</sup>) allowing for greater incorporation into the HOIP and therefore having a larger concentration threshold.

### **C. Effect of metal halide additives on Sn-based HOIP**

Similar to the SrI<sub>2</sub> and MgI<sub>2</sub> additive treatment during the preparation of MAPbI<sub>3</sub> absorbers (discussed above), the addition of SnF<sub>2</sub> to the preparation precursor of Sn-based HOIP absorbers has been reported to improve the performance of resulting solar devices.<sup>51</sup> For a better understanding behind the underlying mechanism of this treatment, the chemical and electronic properties of CsSnBr<sub>3</sub> absorbers with and without the SnF<sub>2</sub> additive were studied via HAXPES by Hartmann et al.<sup>16</sup> Five batches of two samples each (i.e., CsSnBr<sub>3</sub> without and with additive) were measured to monitor for sample reproducibility and to help separate changes detected within samples of a given batch which are due to extraneous factors (e.g., due to unaccounted changes in sample preparation/handling/transporting steps) from those related to the additives. Although some variations between the different batches were found (for more details, please refer to ref. <sup>16</sup>), some significant general changes were detected, which will be discussed next. Figure 5 presents the HAXPES spectra in the shallow core level energy region for one of the measured batches. Whereas both spectra show signal of core levels related to signature elements of the HOIP absorber (i.e., Cs, Sn and Br), only the sample without additive shows additional photoemission lines of elements corresponding to the TiO<sub>2</sub> substrate (i.e., Ti and O), indicating SnF<sub>2</sub>-induced improved absorber coverage throughout the substrate. Comparing the spectra of both samples shows that the peaks of absorber-related core levels of the sample without additive are broader than for the sample with the additive (this is clearly seen in the Sn 4d and Br 3d lines), a sign of a reduction/suppression of Sn<sup>4+</sup> formation and secondary Cs and Br chemical species resulting by the additive. Moreover, inclusion of the additive results in a slight VBM shift

towards  $E_F$  [i.e., from an average  $(1.11 \pm 0.10)$  eV for samples without additive to  $(1.01 \pm 0.10)$  eV]. Considering that oxidation of  $\text{Sn}^{2+}$  to  $\text{Sn}^{4+}$  is reported to lead to p-type doping,<sup>51</sup> the observed change in electronic structure is attributed to a redistribution of Sn 5s-derived states near the  $E_F$  level resulting from the increased  $\text{Sn}^{2+}$  character of the  $\text{CsSnBr}_3$  sample with  $\text{SnF}_2$ .

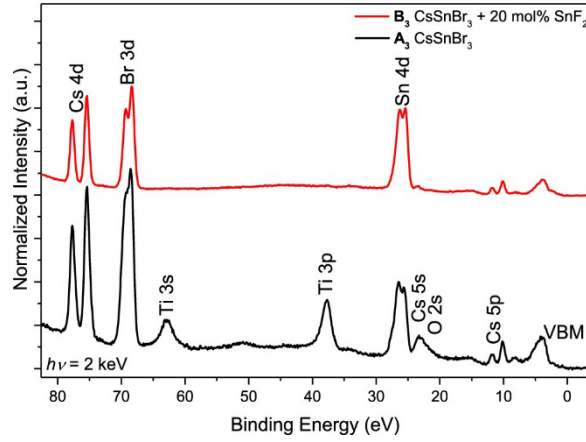


FIG. 5. HAXPES spectra of the shallow core level energy region of  $\text{CsSnBr}_3$  films prepared with and without 20 mol%  $\text{SnF}_2$  additive in the precursor solution on  $\text{TiO}_2$  substrates. An excitation energy of 2 keV was employed. *Reprinted with permission from ref. <sup>16</sup>. Copyright 2020 American Chemical Society.*

## V. EMIL and future steps

The newly built EMIL laboratory combines an intense “tender” x-ray light source – the novel cryogenically cooled in-vacuum undulator U17 – with an APPLE II soft x-ray undulator UE48 to combine HAXPES measurement capabilities with BESSY II’s traditionally strong soft x-ray capabilities into one experimental setup. This two-color

beamline connects to endstations inside a modern material synthesis lab and provides a physical intersection between the HZB's material deposition expertise and its advanced characterization capabilities. Figure 6 displays preliminary data of flux recorded using an ionization chamber with similar settings at the bending magnet KMC-1 beamline and the U17 undulator EMIL beamline. As shown, the intensity provided by the undulator is a significant improvement when compared to the bending magnet KMC-1 beamline. The data are in the expected range and show a significant expansion of the traditionally soft x-ray facility BESSY II towards tender/hard x-ray capabilities. Moreover, the wide angle lens model of the electron analyzer found at EMIL adds an increase in transmission mode of about 3 - 4 times to the recorded intensity when compared to the standard R4000 model (as found at HiKE) significantly enhancing the HAXPES capabilities at BESSY II.

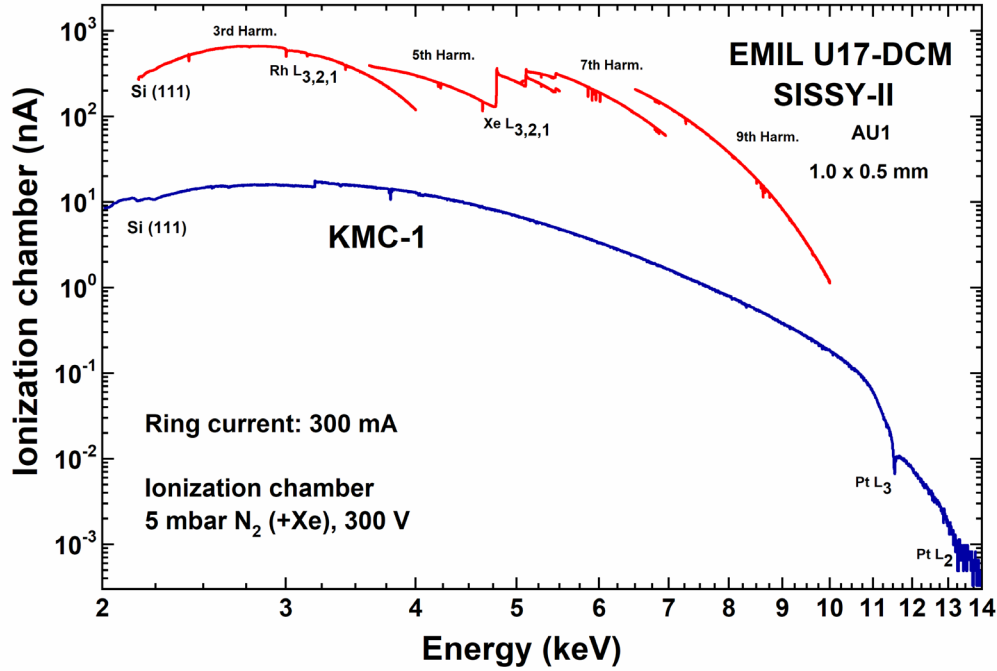


FIG. 6. Comparison of the ionization current recorded at the hard x-ray (U 17) branch of the two color EMIL beamline (red) and the KMC-1 bending magnet beamline (blue) at BESSY II. Both are using a DCM and the same settings of gas type, pressure, and voltage at the ionization chamber, as well as ring current to ensure comparability.

## VI. SUMMARY AND CONCLUSIONS

An overview of recent HAXPES experiments conducted at the HiKE endstation located at the HZB's BESSY II KMC-1 beamline on different sample material systems frequently found in energy conversion devices was presented. Among the findings

revealed by these studies are: the pronounced chemical and electronic structure transformation at the buffer/absorber interface of PDT chalcopyrite samples; origin of performance improvement of solar devices based on kesterite absorbers that have undergone etching and passivation treatments, resulting from removal of secondary chemical phases; determination of structure-function relationship of water oxidation catalysts based on earth-abundant metal oxides; effective tuning of chemical and electronic properties of MoO<sub>3</sub> via sample annealing; determination of band alignment of semiconductor oxide-based heterojunctions; elucidation of mechanisms behind beneficial effects of metal halide additive treatments during HOIP absorber preparation; etc.

Further advancement in related research efforts is anticipated with the new and enhanced HAXPES experimental capabilities of the EMIL facility.

## ACKNOWLEDGMENTS

The authors recognize and are grateful for the supporting role of Charles "Chuck" Fadley, as head of the EMIL International Advisory Committee, in the development and setting up of the EMIL facility and as expert user at HiKE. We also thank Franz Schäfers for making the EMIL U17 and KMC-1 photon flux curves available. The authors thank HZB for the allocation of synchrotron radiation beamtime.

## DATA AVAILABILITY

Raw data were generated at the HZB's BESSY II large scale facility. Derived data supporting the findings of this study are available from the corresponding author upon reasonable request.

## REFERENCES

- <sup>1</sup>M. Gorgoi, S. Svensson, F. Schäfers, G. Öhrwall, M. Mertin, P. Bressler, O. Karis, H. Siegbahn, A. Sandell, H. Rensmo, W. Doherty, C. Jung, W. Braun, and W. Eberhardt, *Nucl. Instrum. Methods Phys. Res., Sect. A* **601**, 48 (2009).
- <sup>2</sup>F. Schaefer, M. Mertin, and M. Gorgoi, *Rev. Sci. Instrum.* **78**, 123102 (2007).
- <sup>3</sup>R. Follath, M. Hävecker, G. Reichardt, K. Lips, J. Bahrtdt, F. Schäfers, and P. Schmid, *J. Phys.: Conf. Ser.* **425**, 212003 (2013).
- <sup>4</sup>S. Hendel, F. Schäfers, M. Hävecker, G. Reichardt, M. Scheer, J. Bahrtdt, and K. Lips, *AIP Conf. Proc.* **1741**, 030038 (2016).
- <sup>5</sup>E. Handick, P. Reinhard, R. G. Wilks, F. Pianezzi, T. Kunze, D. Kreikemeyer-Lorenzo, L. Weinhardt, M. Blum, W. Yang, M. Gorgoi, E. Ikenaga, D. Gerlach, S. Ueda, Y. Yamashita, T. Chikyow, C. Heske, S. Buecheler, A. N. Tiwari, and M. Bär, *ACS Appl. Mater. Interfaces* **9**, 3581 (2017).
- <sup>6</sup>E. Handick, P. Reinhard, R. G. Wilks, F. Pianezzi, R. Félix, M. Gorgoi, T. Kunze, S. Buecheler, A. N. Tiwari, and M. Bär, in: *IEEE 43rd Photovoltaic Specialists Conference (PVSC)*, 2016. IEEE, 2016. - ISBN 978-1-5090-2725-5, pp. 17-21.
- <sup>7</sup>J. Bombsch, E. Avancini, R. Carron, E. Handick, R. Garcia-Diez, C. Hartmann, R. Félix, S. Ueda, R. G. Wilks, and M. Bär, *ACS Appl. Mater. Interfaces* **12**, 34941 (2020).
- <sup>8</sup>N. Nicoara, T. Kunze, P. Jackson, D. Hariskos, R. F. Duarte, R. G. Wilks, W. Witte, M. Bär, and S. Sadewasser, *ACS Appl. Mater. Interfaces* **9**, 44173 (2017).
- <sup>9</sup>B. Vermang, G. Brammertz, M. Meuris, T. Schnabel, E. Ahlswede, L. Choubrac, S. Harel, C. Cardinaux, L. Arzel, N. Barreau, J. van Deelen, P.-J. Bolt, P. Bras, Y. Ren, E.

- Jaremalm, S. Khelifi, S. Yang, J. Lauwaert, M. Batuk, J. Hadermann, X. Kozina, E. Handick, C. Hartmann, D. Gerlach, A. Matsuda, S. Ueda, T. Chikyow, R. Félix, Y. Zhang, R. G. Wilks, and M. Bär, *Sustain. Energy Fuels* **3**, 2246 (2019).
- <sup>10</sup>L. Choubrac, M. Bär, X. Kozina, R. Félix, R. G. Wilks, G. Brammertz, S. Levchenko, L. Arzel, N. Barreau, S. Harel, M. Meuris, and B. Vermang, *ACS Appl. Electron. Mater.* **3**, 5830 (2020).
- <sup>11</sup>J. Pfrommer, A. Azarpira, A. Steigert, K. Olech, P. W. Menezes, R. F. Duarte, X. Liao, R. G. Wilks, M. Bär, T. Schedel-Niedrig, and M. Driess, *ChemCatChem* **9**, 672 (2017).
- <sup>12</sup>S. Y. Smolin, A. K. Choquette, R. G. Wilks, N. Gauquelin, R. Félix, D. Gerlach, S. Ueda, A. L. Krick, J. Verbeeck, M. Bär, J. B. Baxter, and S. J. May, *Adv. Mater. Interfaces* **4**, 1700183 (2017).
- <sup>13</sup>J. Wang, R. G. Wilks, R. Félix, X. X. Liao, A. Grigoriev, and M. Bär, *Adv. Mater. Interfaces* **7**, 2000201 (2020).
- <sup>14</sup>X. Liao, A. R. Jeong, R. G. Wilks, S. Wiesner, M. Rusu, R. Félix, T. Xiao, C. Hartmann, and M. Bär, *ACS Omega* **4**, 10985 (2019).
- <sup>15</sup>N. Phung, R. Félix, D. Meggiolaro, A. Al-Ashouri, G. Sousa e Silva, C. Hartmann, J. Hidalgo, H. Köbler, E. Mosconi, B. Lai, R. Gunder, M. Li, K.-L. Wang, Z.-K. Wang, K. Nie, E. Handick, R. G. Wilks, J. A. Marquez, B. Rech, T. Unold, J.-P. Correa-Baena, S. Albrecht, F. De Angelis, M. Bär, and A. Abate, *J. Am. Chem. Soc.* **142**, 2364 (2020).
- <sup>16</sup>C. Hartmann, S. Gupta, T. Bendikov, X. Kozina, T. Kunze, R. Félix, G. Hodes, R. G. Wilks, D. Cahen, and M. Bär, *ACS Appl. Mater. Interfaces* **12**, 12353 (2020).

- <sup>17</sup>X. Liao, X. Dou, S. N. Habisreutinger, S. Wiesner, G. Sadoughi, D. Abou-Ras, M. A. Gluba, R. G. Wilks, R. Félix, M. Rusu, R. J. Nicholas, H. J. Snaith, and M. Bär, *ACS Appl. Mater. Interfaces* **13**, 17085 (2021).
- <sup>18</sup>R. Félix, W. Witte, D. Hariskos, S. Paetel, M. Powalla, M. Lozac'h, S. Ueda, M. Sumiya, H. Yoshikawa, K. Kobayashi, W. Yang, R. G. Wilks, and M. Bär, *Phys. Status Solidi A* **216**, 1800856 (2019).
- <sup>19</sup>NREL Best Research-Cell Efficiencies. <https://www.nrel.gov/pv/cell-efficiency.html>
- <sup>20</sup>W. Shockley and H. J. Queisser, *J. Appl. Phys.* **32**, 510 (1961).
- <sup>21</sup>D. Schmid, M. Ruckh, F. Grunwald, and H.-W. Schock, *J. Appl. Phys.* **73**, 290 (1993).
- <sup>22</sup>D. Schmid, M. Ruckh, and H.-W. Schock, *Sol. Energy Mater. Sol. Cells* **41–42**, 281 (1996).
- <sup>23</sup>X. Song, R. Caballero, R. Félix, D. Gerlach, C. A. Kaufmann, H.-W. Schock, R. G. Wilks, and M. Bär, *J. Appl. Phys.* **111**, 034903 (2012).
- <sup>24</sup>P. Jackson, R. Wuerz, D. Hariskos, E. Lotter, W. Witte, and M. Powalla, *Phys. Status Solidi RRL* **10**, 583 (2016).
- <sup>25</sup>P. Jackson, D. Hariskos, R. Wuerz, O. Kiowski, A. Bauer, T. Magorian Friedlmeier, and M. Powalla, *Phys. Status Solidi RRL* **9**, 28 (2015).
- <sup>26</sup>A. Laemmle, R. Wuerz, and M. Powalla, *Phys. Status Solidi RRL* **7**, 631 (2013).
- <sup>27</sup>F. Pianezzi, P. Reinhard, A. Chirilă, B. Bissig, S. Nishiwaki, S. Buechelera, and A. N. Tiwaria, *Phys. Chem. Chem. Phys.* **16**, 8843 (2014).
- <sup>28</sup>A. Chirilă, P. Reinhard, F. Pianezzi, P. Bloesch, A. R. Uhl, C. Fella, L. Kranz, D. Keller, C. Gretener, H. Hagendorfer, D. Jaeger, R. Erni, S. Nishiwaki, S. Buecheler, and A. N. Tiwari, *Nature Materials* **12**, 1107 (2013).

- <sup>29</sup>E. Handick, P. Reinhard, J.-H. Alsmeier, L. Köhler, F. Pianezzi, S. Krause, M. Gorgoi, E. Ikenaga, N. Koch, R. G. Wilks, S. Buecheler, A. N. Tiwari, and Marcus Bär, *ACS Appl. Mater. Interfaces* **7**, 27414 (2015).
- <sup>30</sup>S. Siebentritt and S. Schorr, *Prog. Photovoltaics* **20**, 512 (2012).
- <sup>31</sup>S. Chen, X. G. Gong, A. Walsh, and S.-H. Wei, *Phys. Rev. B* **79**, 165211 (2009).
- <sup>32</sup>Z. Huang, D. Ouyang, C. J. Shih, B. Yang, and Choy, *Adv. Energy Mater.* **10**, 1900903 (2019).
- <sup>33</sup>J. Meyer, S. Hamwi, M. Kroger, W. Kowalsky, T. Riedl, and A. Kahn, *Adv. Mater.* **24**, 5408 (2012).
- <sup>34</sup>L. Yang, Y. Xiong, W. Guo, M. Zhou, K. Song, P. Xiao, and G. Cao, *Nano Energy* **44**, 63 (2018).
- <sup>35</sup>M. Si, A. K. Saha, S. Gao, G. Qiu, J. Qin, Y. Duan, J. Jian, C. Niu, H. Wang, W. Wu, S. K. Gupta, and P. D. Ye, *Nat. Electron.* **2**, 580 (2019).
- <sup>36</sup>A. Singh, S. L. Y. Chang, R. K. Hocking, U. Bach, L. Spiccia, *Energy Environ. Sci.* **6**, 579 (2013).
- <sup>37</sup>M. T. Greiner, M. G. Helander, W.-M. Tang, Z.-B. Wang, J. Qiu, and Z.-H. Lu, *Nat. Mater.* **11**, 76 (2012).
- <sup>38</sup>Q.-K. Wang, R.-B. Wang, P.F.-Shen, C. Li, Y.-Q. Li, L.-J. Liu, S. Duhm, and J.-X. Tang, *Adv. Mater. Interfaces* **2**, 1400528 (2015).
- <sup>39</sup>D. F. Pan, G. F. Bi, G. Y. Chen, H. Zhang, J. M. Liu, G. H. Wang, and J. G. Wan, *Sci. Rep.* **6**, 22948 (2016).

- <sup>40</sup>M.-X. Zhou, Z.-W. Li, B. Chen, J.-G. Wan, J.-M. Liu, *J. Phys. D: Appl. Phys.* **46**, 165304 (2013).
- <sup>41</sup>R. G. Wilks and M. Bär, *Nat. Energy* **2**, 16204 (2017).
- <sup>42</sup>W. Ze, S. Zejiao, L. Taotao, C. Yonghua, and H. Wei, *Angew. Chem. Int. Ed.* **56**, 1190 (2017).
- <sup>43</sup>D. Wang, M. Wright, N. K. Elumalai, and A. Uddin, *Sol. Energy Mater. Sol. Cells* **147**, 255 (2016).
- <sup>44</sup>G. Niu, X. Guo, and L. Wang, *J. Mater. Chem.* **3**, 8970 (2015).
- <sup>45</sup>B. Conings, J. Drijkoningen, N. Gauquelin, A. Babayigit, J. D’Haen, L. D’Olieslaeger, A. Ethirajan, J. Verbeeck, J. Manca, E. Mosconi, F. D. Angelis, and H.-G. Boyen, *Adv. Energy Mater.* **5**, 1500477 (2015).
- <sup>46</sup>K. Nishimura, M. A. Kamarudin, D. Hirotani, K. Hamada, Q. Shen, S. Iikubo, T. Minemoto, K. Yoshino, and S. Hayase, *Nano Energy* **74**, 104858 (2020).
- <sup>47</sup>Q. Sun, P. Fassel, D. Becker-Koch, A. Bausch, B. Rivkin, S. Bai, P. E. Hopkinson, H. J. Snaith, and Y. Vaynzof, *Adv. Energy Mater.* **7**, 1700977 (2017).
- <sup>48</sup>N. Aristidou, C. Eames, I. Sanchez-Molina, X. Bu, J. Kosco, M. S. Islam, and S. A. Haque, *Nat. Commun.* **8**, 15218 (2017).
- <sup>49</sup>S. J. Yoon, M. Kuno, and P. V. Kamat, *ACS Energy Letters* **2**, 1507 (2017).
- <sup>50</sup>J. Cao, S. X. Tao, P. A. Bobbert, C. P. Wong, and N. Zhao, *Adv. Mater.* **30**, 1707350 (2018).
- <sup>51</sup>S. Gupta, D. Cahen, and G. J. Hodes, *J. Phys. Chem. C* **122**, 13926 (2018).